A Multiprocess Eyring Model for Large Strain Plastic Deformation

P. Olley, J. Sweeney

School of Engineering Design and Technology, IRC in Polymer Science and Technology, University of Bradford, Bradford BD7 1DP, United Kingdom

Received 2 March 2010; accepted 11 June 2010
DOI 10.1002/app.32951
Published online 27 August 2010 in Wiley Online Library (wileyonlinelibrary.com).

ABSTRACT: A multiprocess Eyring model is developed with a particular aim of predicting the localized instability occurring in "necking" polymers when cold-drawn. Differences from using single and multiple Eyring processes are examined using a published data-set for polypropylene test pieces; it is shown that a four Eyring process model can simultaneously fit both necking stretch ratio and draw force data for uniaxial stretching, whereas with a single process only one measurement could be fitted accurately. The multi process Eyring model is shown to give significantly more accurate predictions than a necking hyperelastic model. The multiprocess model is assessed against the same material undergoing a complex constant-width elongation. It is shown that agreement is quantitatively good for both drawing force and surface deformation, with some minor differences in transverse force and surface stretch. A pronounced intermittent stretching pattern that is seen on the experimental test piece is replicated by the multiprocess Eyring simulation, but is absent using the hyperelastic model. A method is described to deform a photograph of the original specimen according to a finite element solution. The method is shown to give a clear indication of the accuracy of the model in predicting final form. © 2010 Wiley Periodicals, Inc. J Appl Polym Sci 119: 2246–2260, 2011

Key words: eyring; multiprocess; hyperelastic; necking; numerical image deformation

INTRODUCTION

Many industrial processes involve deforming polymers at high temperatures and high strains and take the polymer into strongly nonlinear behavior. The "necking" mechanism, a localized instability exhibited by many polymers when cold-drawn is a particularly challenging phenomenon for a constitutive model and simulation to capture, because many polymers exhibit a large "natural draw ratio" without rupture. Many experimental results for stable necking in polymers have been accounted for by a simple molecular model which explains natural draw ratios and prior-orientation effects in terms of folds in the polymer crystalline regions.[1] Developments from the semicrystalline approach are given by Leonov.[2] The necking process has been studied using a range of hyperelastic models;[3–5] the hyperelastic approach was shown to give good agreement with final neck shape, but the details of drawing force had significant discrepancies. The most significant discrepancy was in the stretch ratio at which yield occurred. In addition, in purely hyperelastic models the physical phenomenon of irreversible deformation is not present, and that a simulated object would revert to its original shape after stretching and release. A range of plastic models have been used in simulations of necking: elastic-plastic yield surface approaches,[6–8] an anisotropic Argon model,[9] an extended Eyring model,[10] and a strain concentration approach.[11] The plastic model of interest in this work is the Eyring model, extended to multiprocess form with multiple Eyring processes operating in parallel, since this is flexible, gives controllable rate dependence, and promises a good replication of drawing force details. The multiprocess Eyring model may be regarded as a general purpose plastic method—it does not attempt to model molecular and structural details of a polymer, but it is a very flexible approach and as will be shown a single parallel elastic process can effectuate the strain-hardening process seen at large strains in semicrystalline polymers.

Application of Eyring process plastic models has been extensive including a wide range of applications in plastics and metals,[12–14] with many other applications, such as geological analysis (see for example Ref. 15). The fundamental Eyring rate model was developed for 3D and shown suitable for application to polymers by Buckley and Jones.[16] Parallel progress was made using the "nucleating" Argon model.[17,18] It was shown by Sweeney et al.[19] that a two process Eyring model gave a significantly better fit to features in the large deformation of

Correspondence to: P. Olley (p.olley@bradford.ac.uk).

polyethylene at 100°C than did a single Eyring process; this was implemented as a "user subroutine" in the ABAQUS simulation package. The number of processes required depends on the particular material and the strain and temperature conditions. Continuing the work with ABAQUS and similar user subroutines, Sweeney et al.[20] showed that a model including a single Eyring process was successful in the prediction of the behavior of a blow-molding grade of polypropylene that deformed uniformly to high multiaxial strains at 135°C. With the same modeling approach at room temperature and smaller, though still substantial strain, Naz et al.[21,22] modeled the constitutive behavior of fracture specimens of ultra-high molecular weight polyethylene, again using a single Eyring process. To give a general capability, in this work the model is extended to a multiprocess Eyring model which allows multiple processes, or "modes," to be superimposed to fit complex deformational behavior; and is implemented in a finite element code. The multiprocess approach promises to be very flexible, and suitable for a wide range of materials showing plastic behavior.

To implement the model a 3D finite element code was developed, using a 3D corotational formulation which is both relatively intuitive and simplifies the action of keeping plastic strain objective under rigid body rotation. The finite element solution method is a Lagrangian-Eulerian method, using a similar mesh and stress update scheme to one used for hyperelastic solution described in Ref. 5. A published data set of large strain rheological experiments is used[4] This data-set is broad enough for a quantitative assessment of the constitutive model and method in one geometry, and then for a challenging cross-test against a different geometry and mode of extension.

EYRING CONSTITUTIVE MODEL

According to the Eyring model, the overall plastic flow rate, $\dot{e}_P$, is determined by a function

$$\dot{e}_P = A \sinh(V_S\ \sigma_{\text{oct}}) \exp(V_P p), \tag{1}$$

which rises sharply when particular values of octahedral stress and pressure are approached, giving plastic yielding. A, V_S, and V_P are constants which control the flow rate, σ_{oct} is the octahedral shear stress, and p is the hydrostatic pressure. Assuming that the plastic flow obeys the Levy-Mises flow rule, flow in the principal directions of stress is given by

$$\frac{\dot{\lambda}_{PJ}}{\lambda_{PJ}} = \frac{\dot{e}_P}{\sigma_{\text{oct}}} \tau_{JJ} \tag{2}$$

where λP_J is the plastic stretch in principal direction J, and τ_{JJ} is the deviatoric stress in the same principal direction.[19] The method provides a well-defined mechanism for plastic flow, and promises to be very suitable for implementation in a multiprocess Eyring form, allowing control over "difficult" behavior such as in necking exhibited by a number of polymer materials.

Corotational formulation

The model can be generalized into an objective 3D model by separating deformation into strain and rotational components. The absolute deformation gradient tensor $\mathbf{F}$ can be written in terms of a symmetrical strain tensor $\mathbf{D}$ and an orthogonal rotation tensor $\mathbf{R}$ such that

$$\mathbf{F} = \mathbf{DR}. \tag{3}$$

The tensor $\mathbf{R}$ can be used to define the localized rotation for a corotational coordinate system.[23] This can be effectuated by the rotation

$$\hat{\mathbf{D}} = \mathbf{R}^{\mathbf{T}}\mathbf{DR} \tag{4}$$

where $\hat{\mathbf{D}}$ is the corotated strain tensor. Effectively strain is rotated with rigid body rotation such that a strain aligned along a given axis of $\hat{\mathbf{D}}$ aligns along the same axis after a rigid body rotation.

The corotated strain tensor can be separated into a elastic component $\hat{\mathbf{D}}_E$ and a plastic component $\hat{\mathbf{D}}_P$ such that

$$\hat{\mathbf{D}} = \hat{\mathbf{D}}_E\, \hat{\mathbf{D}}_P. \tag{5}$$

The change to corotational axes has the effect of making it relatively easy to maintain objectivity of plastic strain under material rotation; a plastic strain which occurs along a given axis before or during rotation, stays aligned (with the material) along the same axis of $\hat{\mathbf{D}}$ after rotation. Considerable "bookkeeping" is saved by this operation. A reverse operation [eq. (11)] returns the corotated stresses to the global (rectangular) axes.

Implementation of multiprocess Eyring model

The multiprocess Eyring model is outlined by Figure 1 with a number of Eyring processes and elastic networks in parallel. One process is purely elastic which allows strain hardening to be accommodated. All parallel processes feel a common strain, and each process reacts according to its set parameters and produces a stress—the addition of these stresses gives the overall stress.

For each time step the change in corotated plastic strain tensor at any given finite element's Gauss point, $\mathbf{d}\hat{\mathbf{D}}_P$, is sought. The total plastic deformation for a given Eyring process, i, is then given by

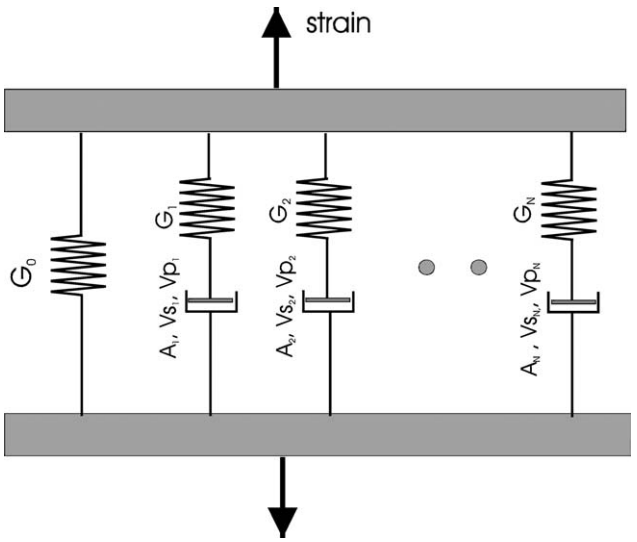

Figure 1 Schematic arrangement of multiprocess Eyring model.

$$\hat{\mathbf{D}}_{Pi} = \mathbf{d}\hat{\mathbf{D}}_{Pi}\,\hat{\mathbf{D}}_{P0,i}, \tag{6}$$

where $\hat{\mathbf{D}}_{P0,i}$ is the plastic deformation tensor for the process at the beginning of the step. When $\hat{\mathbf{D}}_{Pi}$ is known, the elastic deformation gradient tensor for that Eyring process, $\hat{\mathbf{D}}_{Ei}$ is calculated [using eq. (5)] from:

$$\hat{\mathbf{D}}_{Ei} = \hat{\mathbf{D}}\,\hat{\mathbf{D}}_{Pi}^{-1}. \tag{7}$$

The stress in the Eyring process can now be computed. In the present case, the elastic stress model used is the "neo-Hookean" where the strain energy per unit volume for a given Eyring process is given by

$$U = \frac{G_i}{2}(I_1 - 3) - \frac{G_i}{2}\ln(I_3) + \frac{\beta}{2}G_i(\ln(I_3))^2, \tag{8}$$

where G_i is the shear modulus associated with Eyring mode i, and I_1 and I_3 are the first and third invariants of the left Cauchy-Green deformation tensor, $\hat{\mathbf{B}}_i$, where $\hat{\mathbf{B}}_i = \hat{\mathbf{D}}_{Ei}\,\hat{\mathbf{D}}_{Ei}^{\mathbf{T}}$. The second term in eq. (8) serves to remove the "artefact" pressure at zero strain, whilst the third term adds a pressure equal to $-2\beta G_i \ln(I_3)$ to resist volume changes.

When U is considered as a function of the invariants of $\hat{\mathbf{B}}_i$ (I_1, I_2, and I_3) the principal stresses are given by

$$\sigma_{JJ}^{123} = 2\left[\lambda_J^2\frac{\partial U}{\partial I_1} - \frac{1}{\lambda_J^2}\frac{\partial U}{\partial I_2} + I_3\frac{\partial U}{\partial I_3}\right], \tag{9}$$

where σ_{JJ}^{123} is the stress in principal direction J (for any given Eyring mode); λ_J^2 is the square of the stretch ratio in principal direction J, equal to Eigenvalue J of $\hat{\mathbf{B}}_i$. The stresses for Eyring mode, i, in the principal directions, σ_i^{123} can then be rotated back to the corotational coordinate system

$$\hat{\sigma}_i = \mathbf{M}\,\sigma_i^{\mathbf{123}}\,\mathbf{M}^{\mathbf{T}} \tag{10}$$

where $\mathbf{M}$ is a rotation matrix whose columns are the Eigenvectors of $\hat{\mathbf{B}}_i$, and $\hat{\sigma}_i$ is the stress in the corotated coordinate system.

The multiprocess Eyring model comprises a neo-Hookean network [eq. (8)] and a number of Eyring networks in parallel, such that each network experiences the same absolute deformation, the stresses of these networks add to give the overall stress. The total Cauchy stress in the global (rectangular) coordinate system, $\Omega^{\mathbf{xyz}}$, is now obtained from the summation of all Eyring modes (and the neo-Hookean mode) rotated back from the corotational to the global frame of reference:

$$\Omega^{\mathbf{xyz}} = \sum \mathbf{R}\,\hat{\sigma}_i\mathbf{R}^{\mathbf{T}}. \tag{11}$$

Determining the plastic strain

To determine the elastic strain, the plastic strain must be known. The increment in plastic strain over the time step, $\mathbf{d}\hat{\mathbf{D}}_{Pi}$, must be found and combined with the total plastic strain at the beginning of the step, $\hat{\mathbf{D}}_{P0i}$, to determine the plastic strain at the end of the time step. To compute the plastic strain increment the absolute deformation gradient tensor, $\mathbf{F}$ is split using a left polar decomposition according to $\mathbf{F} = \mathbf{DR}$ [eq. (3)], where $\mathbf{D}$ is a symmetric stretch tensor and $\mathbf{R}$ is a rotation tensor.[24] The stretch tensor can be computed from $\mathbf{F}$ using

$$\mathbf{D} = \left(\mathbf{FF}^{\mathbf{T}}\right)^{\frac{1}{2}}. \tag{12}$$

The rotation tensor is directly computed using $\mathbf{R} = \mathbf{D}^{-1}\mathbf{F}$. The corotated strain tensor, $\hat{\mathbf{D}}$, is then obtained from $\hat{\mathbf{D}} = \mathbf{R}^{\mathbf{T}}\mathbf{DR}$ [eq. (4)].

Each Eyring network is subject to the same corotated stretch tensor $\hat{\mathbf{D}}$. For a given Eyring mode, indicated by the index i, we have

$$\hat{\mathbf{D}}_{Pi} = \mathbf{d}\hat{\mathbf{D}}_{Pi}\,\hat{\mathbf{D}}_{P0i}, \tag{13}$$

where $\hat{\mathbf{D}}_{P0i}$ is the total plastic deformation at the beginning of the step. $\mathbf{d}\hat{\mathbf{D}}_{Pi}$ is arrived at by an iterative process; denoting the iterations by the index, k, we introduce a trial plastic deformation change over a time step $\mathbf{d}\hat{\mathbf{D}}_{Pi,k}$, where the starting estimate for the first iteration can be taken as the identity matrix $\mathbf{I}$.

This gives a trial total plastic deformation at iteration k of the time step of

$$\hat{\mathbf{D}}_{P_{i,k}} = \mathbf{d}\hat{\mathbf{D}}_{P_{i,k}}\,\hat{\mathbf{D}}_{P0_i}. \tag{14}$$

The trial elastic strain of that mode $\left(\hat{\mathbf{D}}_{E_{i,k}}\right)$ is then computed [making use of eq. (7)] as

$$\hat{\mathbf{D}}_{E_{i,k}} = \hat{\mathbf{D}}\left(\hat{\mathbf{D}}_{P_{i,k}}\right)^{-1}. \tag{15}$$

The stress in the principal coordinate system, σ^{123}, can now be evaluated by computing a Cauchy-Green tensor $\hat{\mathbf{B}}_{E_{i,k}} = \hat{\mathbf{D}}_{E_{i,k}}\left(\hat{\mathbf{D}}_{E_{i,k}}\right)^{\mathrm{T}}$ and proceeding as given by eqs. (8) and (9).

From σ^{123}, the octahedral stress can now be computed from

$$\sigma_{\mathrm{oct}} = \left(\frac{1}{3}\left(\left(\tau_{11}^{123}-\tau_{22}^{123}\right)^2+\left(\tau_{11}^{123}-\tau_{33}^{123}\right)^2\left(\tau_{22}^{123}-\tau_{33}^{123}\right)^2\right)\right)^{\frac{1}{2}}, \tag{16}$$

where τ^{123} is a deviatoric stress in the principal directions given by.

$$\tau_{JJ}^{123} = \sigma_{JJ}^{123} - \frac{1}{3}\mathrm{trace}\left(\sigma^{123}\right) \tag{17}$$

For an Eyring process identified by index i (neglecting flow due to hydrostatic pressure) the plastic rate is

$$\dot{e}_{P_i} = A_i\,\sinh\left(V_{S_i}\,\sigma_{\mathrm{oct}}\right). \tag{18}$$

In the case that plastic deformation over the time step is colinear with the current stress tensor, eq. (2) gives

$$\lambda_{P_J}\big|_{t+\Delta t} = \lambda_{P_J}\big|_t \exp\left(\frac{\dot{e}_{P_i}\tau_{JJ}}{\sigma_{\mathrm{oct}}}\Delta t\right), \tag{19}$$

allowing the stretches for principal directions $J = 1,2,3$ to be computed over the time-step. This allows the relative change in principal stretch ratios to be calculated from

$$\delta\lambda_{P_J} = \lambda_{P_J}\big|_{t+\Delta t} \Big/ \lambda_{P_J}\big|_t = \exp\left(\frac{\dot{e}_{P_i}\tau_{JJ}}{\sigma_{\mathrm{oct}}}\Delta t\right). \tag{20}$$

Although in general deformations plastic deformation is not guaranteed to be colinear with current stress, we use the expression

$$\delta\lambda_{P_J} = \exp\left(\frac{\dot{e}_{P_i}\tau_{JJ}}{\sigma_{\mathrm{oct}}}\Delta t\right) \tag{21}$$

as it keeps plastic deformation increments along the principal directions of the current stress, keeps the determinant of the plastic strain tensor at unity, and reduces to the colinear case for colinear stress and plastic deformation.

The stretch changes, $\delta\lambda_P$, are then rotated back to the corotational coordinate system of $\hat{\mathbf{D}}_{E_{i,k}}$ to give the updated plastic strain increment for process i at iteration $k+1$, $\mathbf{d}\hat{\mathbf{D}}_{P_{i,k+1}}$, using

$$\mathbf{d}\hat{\mathbf{D}}_{P_{i,k+1}} = \mathbf{M}_k\,\delta\lambda_P\,\mathbf{M}_k^{\mathbf{T}}, \tag{22}$$

where $\mathbf{M}_k$ is a rotation matrix whose columns are the Eigenvectors of $\hat{\mathbf{B}}_{E_{i,k}}$. From eq. (17) it is clear that $\tau_{11}^{123} + \tau_{22}^{123} + \tau_{33}^{123} = 0$, use of eq. (21) thus guarantees unity determinant in $\delta\lambda_P$.

It was found necessary to introduce relaxation into the evolution of the plastic strain increment for the iterations (k) within a time-step. To keep unity determinant, the under-relaxation was accomplished using application of the function:

$$\mathbf{d}\hat{\mathbf{D}}'_{P_{i,k+1}} = \left(\mathbf{d}\hat{\mathbf{D}}_{P_{i,k+1}}\right)^{\theta}\left(\mathbf{d}\hat{\mathbf{D}}_{P_{i,k}}\right)^{1-\theta} \tag{23}$$

where θ is a relaxation factor. A value of $\theta = 0.1$ was used throughout this work.

Efficient computation of Eigenvalues, Eigenvectors, and powers of tensors

Computing subunity powers and the Eigenvectors of symmetrical 3×3 tensors has proven to be the greatest part of computational cost for this model; in view of this tests were carried out on a number of published codes for QR, Jacobi and tridiagonalization methods. Attention is drawn to a recent publication by Kopp[25] which gives an efficient analytical method for finding Eigenvalues and Eigenvectors of symmetric 3×3 matrices. Our tests found this method considerably faster than any other method tried, and equally robust. These algorithms (to be precise the "hybrid" code of Kopp available at http://www.mpi-hd.mpg.de/~globes/3x3/) were used for all Eigen computations throughout this work. A method is available for computing powers of tensors using Eigenvalues and Eigenvectors.[24]

FINITE ELEMENT SOLUTION METHOD

Stresses in the Eyring model are computed numerically, rather than in terms of displacements as for the small strain linear stress model. Having the Cauchy stress in the global frame of reference, Ω^{xyz} (which is henceforth written as Ω for simpler notation), the method proceeds from Cauchy's equation of motion with inertia neglected:

$$0 = \nabla \cdot \Omega + \mathbf{f} \tag{24}$$

We proceed to develop an implicit solution method employing a notional small strain stiffness matrix; this method is adapted from a method first used for the solution of viscoelastic flows by Viriyayuthakon and Caswell.[26] To introduce an implicit method, the force-balance of notional small-strain stresses, given by $\nabla \cdot (G\,\mathbf{e_G}\mathbf{u} + B\mathbf{e_B}\mathbf{u})$, is subtracted from each side of the equation. G is a shear modulus comparable to the low-strain shear modulus of the nonlinear constitutive model, and B is a bulk modulus. $\mathbf{e}_G$ and $\mathbf{e}_B$ are the small-strain deviatoric and spherical stress operators respectively [$\mathbf{e_G} = \mathbf{A}$, and $\mathbf{e_B} = \mathbf{C}$, where $A_{ij} = \partial u_i/\partial x_j + \partial u_j/\partial x_i$ and **C**is a diagonal matrix with entries $C_{ii} = \partial u_i/\partial x_i$ (summation implied)]. An iterative process is introduced by subtracting the known values at iteration k from the RHS of the equation, and the unknown values at iteration $k + 1$ from the LHS of the equation; upon convergence this is equal to subtracting the same quantity from each side. This gives

$$-\nabla \cdot (G\,\mathbf{e_G}\mathbf{u}_{k+1} + B\mathbf{e_B}\mathbf{u}_{k+1}) = \nabla \cdot (\Omega - G\,\mathbf{e_G}\mathbf{u}_k - B\mathbf{e_B}\mathbf{u}_k) + \mathbf{f} \quad (25)$$

The standard finite element procedure of multiplication by the interpolation functions ψ_i, and integration over the problem domain leads to

$$\mathbf{K}\mathbf{u}_{k+1} = \mathbf{F}, \quad (26)$$

where

$$\mathbf{K} = \int_V [\nabla \cdot \psi_i]\,(G\,\mathbf{e_G} + B\mathbf{e_B})\,dV, \quad (27)$$

and

$$\mathbf{F} = \int_S \psi_i\,\mathbf{f}\,dS - \int_V [\nabla \cdot \psi_i]\,(\Omega - G\,\mathbf{e_G}\mathbf{u}_k - B\mathbf{e_B}\mathbf{u}_k)\,dV. \quad (28)$$

For simulation purposes, it is convenient to set $G = \omega G'$, where G' is the small-strain shear modulus of the constitutive model (equal to the sum of all G_i). The parameter ω is a relaxation parameter, a value of 5 was found just sufficiently high to obtain convergence for the problems studied. In view of the choice of penalty pressure [in eq. (8)], an appropriate choice for the bulk modulus, B, is $B = 2\beta G'$, since this gives a stiffness matrix of comparable "stiffness" to the "forces" due to the penalty pressure. If required the pressure p can be evaluated using $p = -2\beta G' \ln(I_3)$, where I_3 is the third invariant of the Cauchy-Green tensor [using eq. (8)]. This leads to

$$\mathbf{K}'\,\mathbf{u}_{k+1} = \mathbf{F}', \quad (29)$$

where

$$\mathbf{K}' = G' \int_V [\nabla \cdot \psi_i]\,(\omega\,\mathbf{e_G} + 2\beta\mathbf{e_B})\,dV, \quad (30)$$

and

$$\mathbf{F}' = \int_S \psi_i\,\mathbf{f}\,dS - \int_V [\nabla \cdot \psi_i]\,(\Omega - \omega\,G'\,\mathbf{e_G}\mathbf{u}_k - 2\beta\,G'\mathbf{e_B}\mathbf{u_k})\,dV. \quad (31)$$

Thus eq. (31) is evaluated using the latest stresses and deformations at the start of each iteration, and is input as a force vector into eq. (29), to give updated displacements, $\mathbf{u_{k+1}}$. Each time-step thus follows an iterative procedure, whereby trial solution $k + 1$ is computed using trial stresses and displacements from solution k, until convergence. The nodal positions of the mesh are updated after each iteration according to

$$\mathbf{X}'_{k+1} = \mathbf{X^0} + \mathbf{u}_{k+1}, \quad (32)$$

where $\mathbf{X^0}$ is the undeformed mesh, and $\mathbf{X}'_{k+1}$ is the latest deformed mesh. Upon convergence, $\mathbf{u}_{k+1} = \mathbf{u}_k$, and a the notional small-strain stresses cancel, to leave the solution one time step advanced.

IMPLEMENTATION AND SIMULATION PROCEDURE

The Eyring process was implemented using eight-noded "brick" finite elements with displacement components at the nodes. Three-point Gaussian integration was used (i.e., 27 Gauss points per element). The total stress was computed at each Gauss point [i.e., the stress given by eq. (11)], and the system of equations assembled according to eqs. (29)–(31). The pressure penalty factor, β, needs to be as low as possible to prevent mesh failure without inhibiting (by partial "mesh locking") the deformation induced by the constitutive model. A value for the penalty factor, β, of 30 was needed to prevent mesh failure for the uniaxial test specimen (reported later) with a value of 10 being sufficient for the planar extension test specimen. Pressure dependent slip rate was omitted in all cases [setting $V_p = 0$ in eq. (1)]. An incremental load procedure was used such that enforced stretching boundary conditions gave an average strain increase of around 2% per time step; the time step was chosen to give the extension rate of the process under consideration. Over each time step, the iterative procedure was applied over a number of iterations, k; in one whole iteration the updated trial displacements and mesh position were computed according to eqs. (29)–(32), followed by

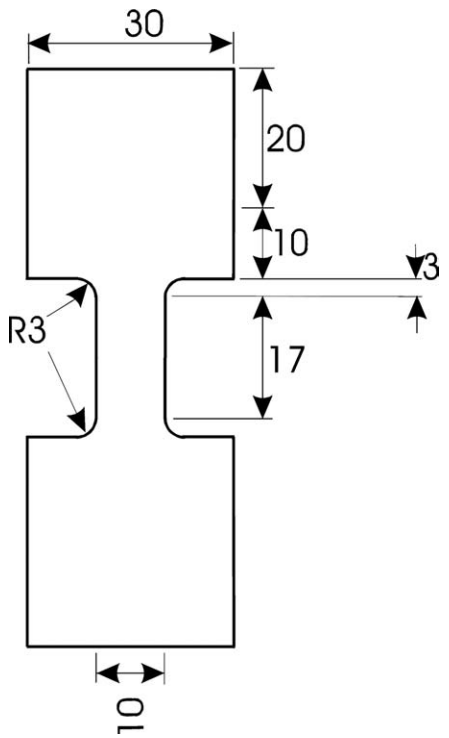

Figure 2 Geometry of 1.6 mm thick plane test specimen. All dimensions in mm.

computation of the trial plastic deformation for each Eyring mode, i [using eqs. (14)–(18) and (21)–(23)]; with the trial plastic deformation new trial Cauchy stresses and mesh position could be calculated using eqs. (7), (9), (10), and (32). This was iterated until convergence criteria was met, in this work the criteria used was $\Delta u/U < \varepsilon$, where Δu is the largest iteration-to-iteration change in any nodal displacement component, U is a characteristic displacement, and ε is a "small" number—a value of 1×10^{-4} was used in this work.

Uniaxial extension test specimen

The simulation was applied to a uniaxial extensional problem for which published experimental data is available.[4] The polypropylene used was in sheet form, manufactured by Tiszai Vegyi Kombinat, Hungary and known as grade K-899. The tensile test piece is shown in Figure 2. The specimen with a 17 mm long narrow cross section was stretched at 150°C by a further 35 mm at a constant velocity, with an initial stretch rate of 0.014 s^{-1} (0.24 mm s^{-1}). The force required to stretch was recorded against extension in Ref. 4. Initially a single Eyring process was used, along with a parallel neo-Hookean process to see if force/extension data could be fitted accurately from a single Eyring mode. Preliminary runs of the simulation were required to establish Eyring constants; a value of 6×10^{-15} s^{-1} for A was chosen as a base value as it gives an increase of 5% in peak stretching force for a factor of 4 rise in stretching rate as reported.[4] A characteristic noted through these preliminary runs is that small values of $A_i (\sim 10^{-12}$ or lower) were found to be needed for necking to occur. An interpretation is that a small value of A means that a large value of V_S is needed to give the correct peak stress; as V_S sets the exponential rate within the (exponentially based) sinh function [eq. (1)], then any rise in stress gives a large plastic flow rate, and local instability is encouraged. The parameter values that were used are given in Table I.

It is interesting to compare the plastic Eyring model with a (purely elastic) necking hyperelastic model used in Refs. 4 and 5. This model is a modification of the Ball Model of Ball et al.[3], and is defined by the energy function:

$$U = \frac{1}{2}N_C I_1 + \frac{1}{2}N_S \left[\frac{(1+\eta)\left(I_1 + 2\eta I_2 + 3\eta^2\right)}{1 + \eta I_1 + \eta^2 I_2 + \eta^3} + \ln\left(1 + \eta I_1 + \eta^2 I_2 + \eta^3\right)\right], \quad (33)$$

where N_C and N_S are related to the density of crosslinks and sliplinks in the polymer, respectively, and η is a parameter defining the extent of motion of the sliplinks.[4] N_S is defined as

$$N_S(I_1) = \frac{N_{S0} - N_{S\infty}}{(I_1 - 2)^{\alpha}} + N_{S\infty} \quad (34)$$

where N_{S0} is the initial value of N_S, and $N_{S\infty}$ is the limiting value at large strains; α controls the rate of change from the initial to limiting value. The parameters used were $N_C = 0.33$ MPa, $N_{S0} = 6.64$ MPa, $N_{S\infty} = 2.13$ MPa, $\eta = 0.2$, and $\alpha = 2.0$. For direct comparison this model was implemented in the multiprocess Eyring code by three changes: (i) using only one process; (ii) replacing the neo-Hookean part of the energy function [eq. (8)] with eq. (33), and (iii) setting the plastic flow controlling parameter, A, to zero.

Figure 3 compares the experimentally obtained nominal stress (stretching force/initial cross section) with the corresponding results from simulation. The stretch ratio is a nominal stretch ratio given by

TABLE I
Parameters Used for Single Eyring Mode Simulations with "Small A_1"

Mode	G_i (Pa)	A_i (s^{-1})	V_s (Pa^{-1})
Eyring mode $i = 1$	9×10^6	6×10^{-15}	12.7×10^{-6}
Neo-Hookean	3×10^5	–	–

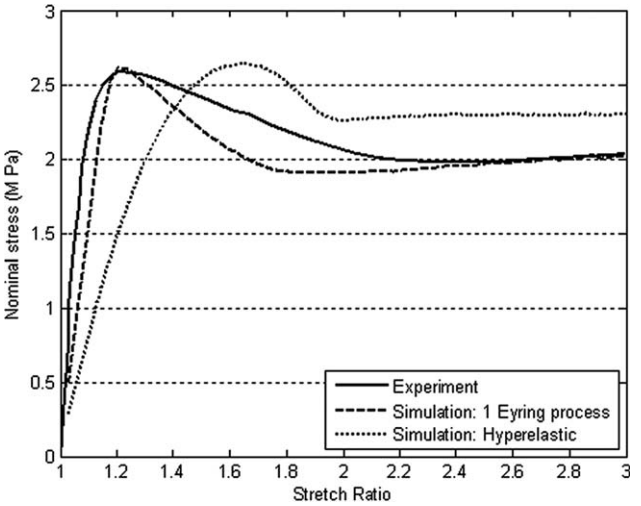

Figure 3 Comparison between experiment at an initial stretch rate of 0.014 s^{-1} and simulations using a single Eyring process, and using a necking hyperelastic model.

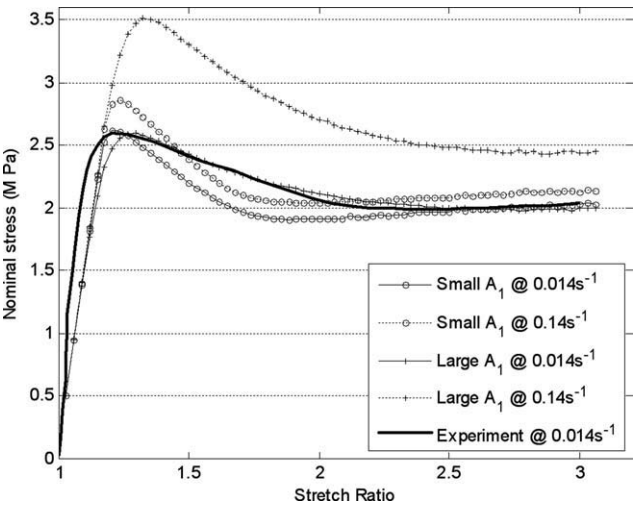

Figure 4 Simulation at two initial stretch rates using a single process Eyring fit with "small" A_1 (6×10^{-15} s^{-1}) and "large" A_1 (6×10^{-5} s^{-1}).

$(L + L_0)/L_0$, where L is the extension, and L_0 is the original length of the narrow section (17 mm). It is seen that the height of the peak is matched well by both simulations, although only the Eyring model matches the position of the experimental peak well. The overall shape from the single process Eyring model is similar to experiment, but suggests that using multiple Eyring modes may improve capability to fit the data. A much larger value of A_1, 6×10^{-5} s^{-1}, was able to gave a very good fit to the stretching force data at 0.014 s^{-1}, although the change in peak stress with stretching rate was greatly over-predicted. We refer to the two parameter sets as "large A_1" and "small A_1." The parameters used for "large A_1" are summarized in Table II.

Figure 4 compares the simulated nominal stress using the Eyring model with both sets of parameters at extension rates of 0.014 s^{-1}, and 0.14 s^{-1}. The curve for large A_1 at 0.014 s^{-1} is very close to experimental data, the drop-off rate after the peak matches the drop off rate from experiment. At the higher stretch rate it is noticeable that the large A_1 curve shows most change due to rate, this is to be expected due to increased rate dependency with increasing value of parameter A, as shown by several analyses (e.g., Ref. 19). Although the "large A_1" simulation matches the data at the experimental rate of 0.014 s^{-1}, the increase in stress level with extension rate is approximately four times higher than reported in Ref. 4. Another difference from experiment is seen when the specimen deformation is studied. Experimentally, the material readily "necks" under elongational stretching. Figure 5 shows the front surface of the meshes at the end of stretching for "small A_1," and "large A_1" parameter sets. Necking is pronounced using the small A_1 parameter set, similar to experimental results, but is absent from

TABLE II
Parameters Used for Single Eyring Mode Simulations with "Large A_1"

Mode	G_i (Pa)	A_i (s^{-1})	V_s (Pa^{-1})
Eyring mode $i = 1$	9×10^6	6×10^{-15}	2.65×10^{-6}
Neo-Hookean	3×10^5	–	–

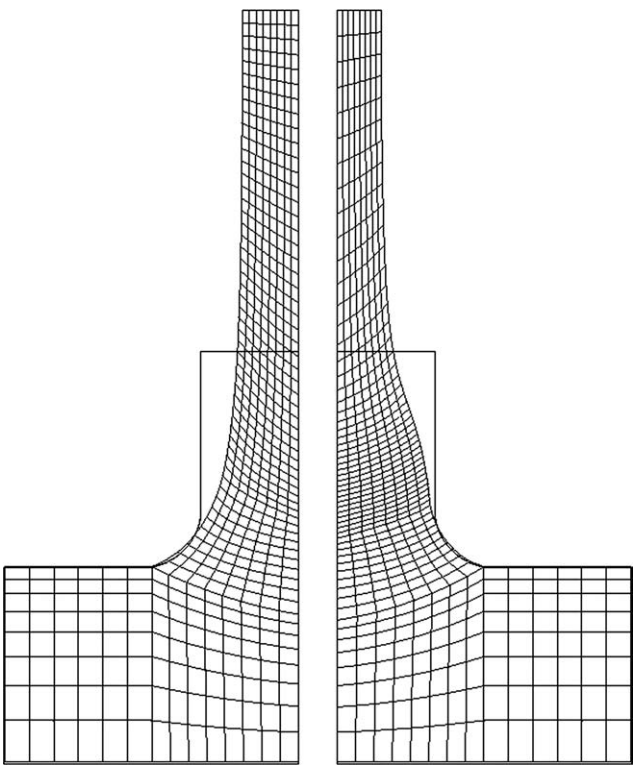

Figure 5 Comparison on predicted stretching using large A_1 (left) and small A_1 (right).

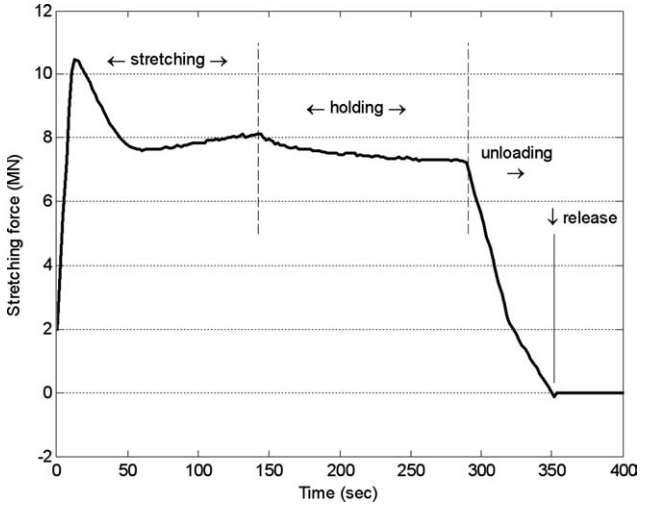

Figure 6 Simulated stretching force during the extension, holding, and gradual releasing of the specimen.

results with the large A_1 parameter set; quantitative comparisons are made later in this work. The situation was largely repeated at the higher stretch rates, with more pronounced necking using the "small A_1" parameter set, but again no necking using the "large A_1" parameter set.

The extent of permanent deformation from the Eyring model was investigated by removing stretching forces after pulling. The simulation stretched the sample at a rate of 0.014 s^{-1}; after this phase a 'holding' phase was enforced in which the sample was held in the final stretched position for a time equal to total stretching time. After this followed an "unloading" phase in which the enforced stretch is reduced at the same rate as it was applied. Reaction force (due to the stretching boundary conditions) was monitored during this time; when the reaction force first reached below zero, the stretching boundary conditions were removed completely and the part allowed to settle into a final shape. Figure 6 shows the plot of stretching force against time during this operation. Stress relaxation can be seen, during the 'holding' time, to be a slow process after a fast initial drop (since the stress rapidly drops out of the high "exponential" rate of the Eyring process). Negligible change in the mesh was observed after the first few time steps following the removal of the stretching boundary conditions. Figure 7 compares the mesh after the end of initial stretching, and the mesh after being released. After unloading a reduction of around 40% stretch is seen, though clearly different cooling and 'holding time' sequences would strongly affect this value. The result confirms that the Eyring model gives a permanent plastic deformation in the test piece, this is in contrast to results obtainable from the necking hyperelastic model in which the mesh must return to its initial shape on release.

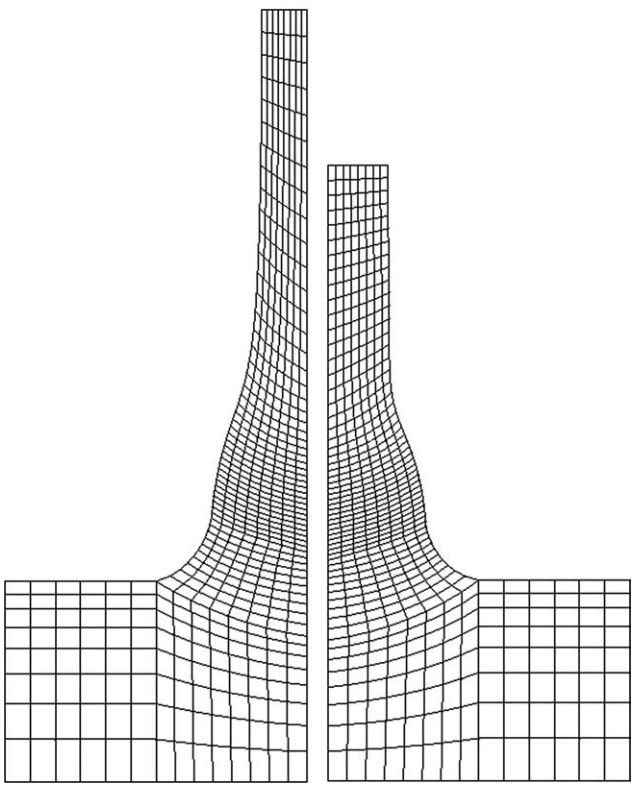

Figure 7 Comparison of front face of mesh at the end of the stretching phase (left) and after unloading and releasing (right).

TABLE III
Parameters Used for Four Eyring Mode Simulations

Mode	G_i (Pa)	A_i (s^{-1})	V_s (Pa^{-1})
Eyring mode $i = 1$	11.0×10^6	6×10^{-15}	1.88×10^{-5}
Eyring mode $i = 2$	1.8×10^6	6×10^{-15}	5.6×10^{-5}
Eyring mode $i = 3$	4×10^5	6×10^{-15}	1.2×10^{-4}
Eyring mode $i = 4$	1.5×10^5	6×10^{-15}	5.8×10^{-5}
Neo-Hookean	2.5×10^5	–	–

Application of multimode Eyring process

As seen in Figure 4, a single Eyring process with a large value of "A_1" gave a good fit to experimental force data at one rate, but gave negligible necking. The smaller value of "A_1" gave necking, and also gave the correct experimental rise in peak stress with stretching rate, but didn't produce the overall

TABLE IV
Parameters Used for Two Eyring Mode Simulations

Mode	G_i (Pa)	A_i (s^{-1})	V_s (Pa^{-1})
Eyring mode $i = 1$	9×10^6	6×10^{-15}	1.35×10^{-15}
Eyring mode $i = 2$	3×10^6	6×10^{-15}	7.5×10^{-5}
Neo-Hookean	2.7×10^5	–	–

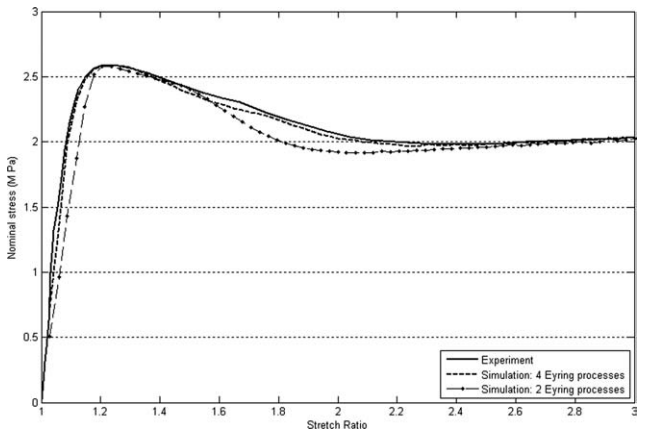

Figure 8 Experimental nominal stress for the uniaxial test specimen compared with simulation using 2 and 4 Eyring processes.

correct shape for stretching force. To see if force could be fitted using several Eyring processes, and if this fit could give a useful prediction of other experimental necking data, multiple Eyring processes were used with the value of A_1 fixed at 6×10^{-15} s^{-1} to match the known rate dependence. It was found that four Eyring processes in parallel with a single fixed neo-Hookean gave a good fit to the observed stretching force. The parameters used are listed in Table III. Parameters for a fit using two Eyring processes are given in Table IV.

The nominal stress from the simulation using four Eyring modes is compared to the experimental data in Figure 8. It is seen that the details of the experimental data are well replicated, with an accurate initial rise rate, position of peak stress, and behavior after the peak. The two Eyring process model can be seen to fit the experimental data better than the single Eyring process model (Fig. 3), but substantially less well than the four process model. The maximum difference using four Eyring processes is $\sim$ 2%. This demonstrates, so far, that a close fit to stretching force data is possible with the multiprocess Eyring model. The model's predictive ability is now examined.

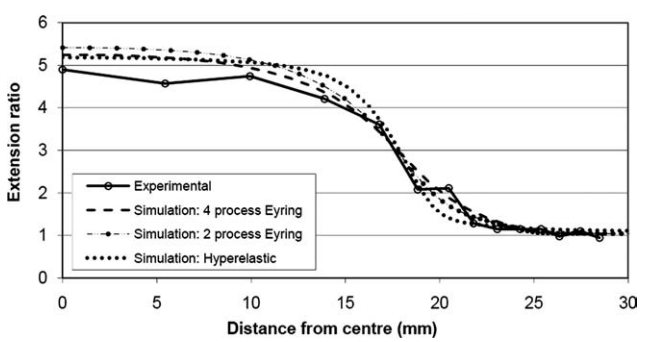

Figure 9 Comparison of surface stretch ratio along the specimen from experiment, 4 and 2 process Eyring models, and hyperelastic model.

The measured centre line surface stretch is available[4] and a quantitative comparison with the simulation results for the two and four-process Eyring models and also for the "necking" hyperelastic model [eq. (33)] is shown in Figure 9. The overall agreement from all simulations is good with the four-mode Eyring and hyperelastic models giving a peak stretch ratio at the centre of 5.2, comparing with 4.9 from experiment. The two-mode Eyring model gives a slightly higher peak stretch ratio of 5.4. These values are significant as they represent the "natural draw ratios" of the constitutive models and the physical material, respectively. The distance from the centre at which necking develops is closely matched by all models, with a slightly better match to the rise rate from the Eyring models. The structural deformation occurring in the test piece simulated by the four-process Eyring model is shown in Figure 10; a distinct neck is predicted as expected.

The contribution to stress of each Eyring process (in the four process model) can be gauged from Figure 11 which shows the deviatoric stress from each mode in the direction of stretching at an element in the centre of the high stretch region. These deviatoric stresses are compared with the experimental apparent stress (which also includes the contribution of pressure). It can be perceived how the individual modes add to give approximately the shape of experimental data.

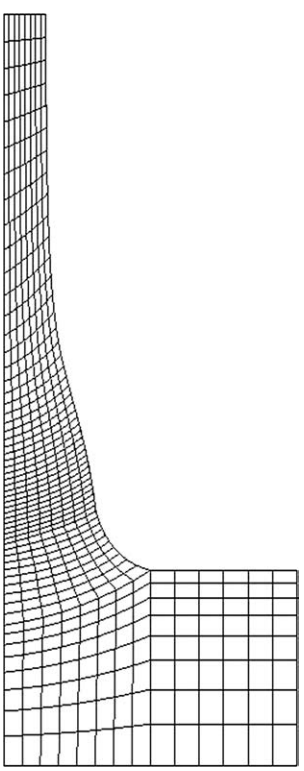

Figure 10 Back plane of 3D mesh after stretching using 4 Eyring processes.

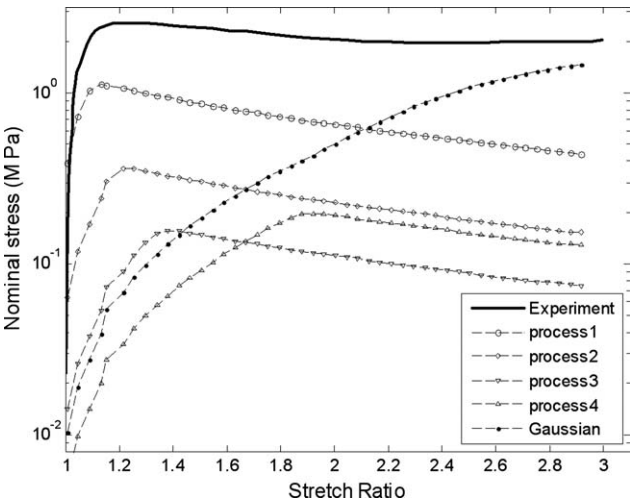

Figure 11 Deviatoric stress for each Eyring process in the direction of bulk stretch indicating each process's contribution to nominal stress.

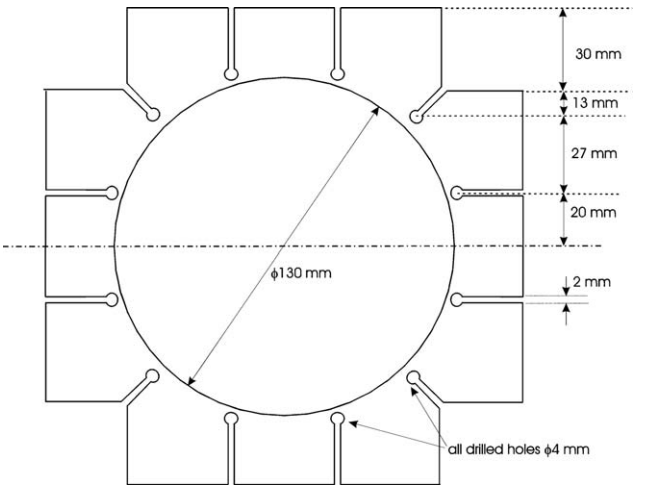

Figure 12 Geometry of Biaxial test specimen. Thickness is 1.6 mm with central circle machined to 0.8 mm thickness.

Unlike the single mode Eyring model, a multimode model is shown to capture both drawing force details, and necking with good accuracy; four processes were needed for this data set. The rise in peak stress with stretching rate is also captured by use of the "Small A_1" parameter set.

Planar test specimen

Results from a planar extension experiment using the same material and temperature are available.[4] To be broadly useful, a constitutive model should work for planar deformation using material constants found from uniaxial tests; thus cross-comparing against a planar experiment represents a critical test for a constitutive model. In the planar experiment a square sheet was stretched at a constant rate in one direction, whilst applying a force in the transverse direction such that a constant width was maintained. Figure 12 shows the test specimen geometry, and Figure 13 shows the test specimen, printed with a 5 mm grid of squares before extension. Figure 14 shows a specimen after being stretched to an overall draw ratio of 2.2 at an initial extension rate, $\dot{e}$ of 0.014 s^{-1}. (defined by $\dot{e} = \dot{L}/L_0$ where $\dot{L}$ is the constant extension rate (mm/s) and L_0 is the 130 mm diameter of the planar deformation material). It can be seen that the deformation is complex with intermittent stretch: small stretch ratios between the areas supported by a thicker section, and necking where there is no support.

Stretching forces were compared. The experiment was repeated several times with the upper and lower limits given for nominal stress in both the axial direction (direction of stretching) and the transverse direction.[4] The nominal stress is the total force in a direction divided by the initial area of the thinner section (130 mm $\times$ 0.8 mm for both). The simulation results for both four-process Eyring and Hyperelastic models are compared with the published experimental results in Figure 15. The axial stresses from both models match well in terms of peak value, although only the Eyring model gives the peak value at the correct stretch ratio. However the Eyring simulation gives nominal stress below experiment at stretch ratios above 1.4. The transverse stress simulated using the Eyring model is always within the upper and lower experimental limits; the hyperelastic model again only reaches the correct level above a stretch ratio of $\sim$ 1.4. Considering the major differences in geometry and testing machines

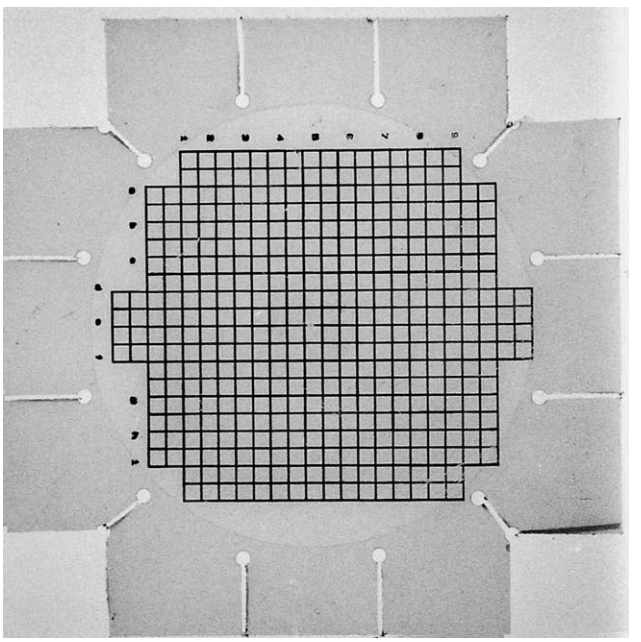

Figure 13 Photograph of full undeformed specimen.

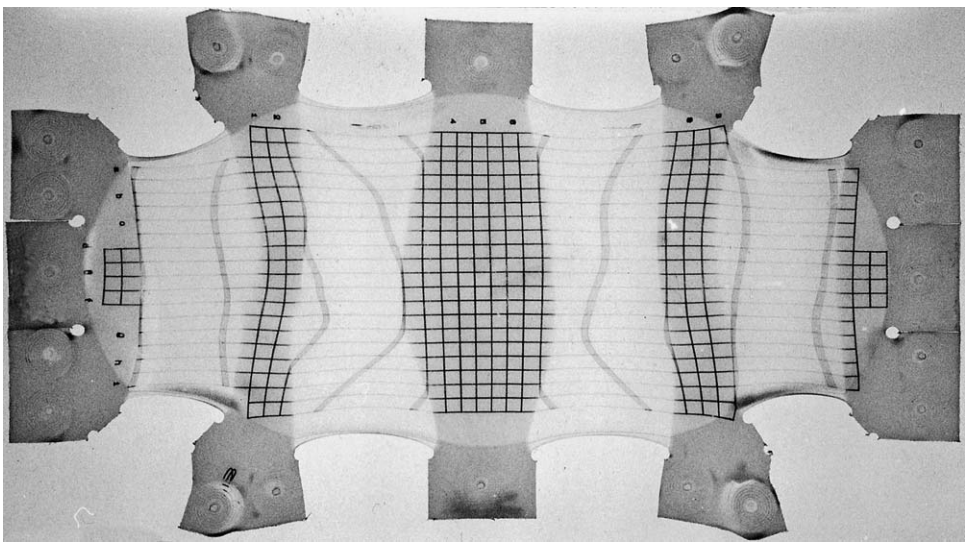

Figure 14 Photograph of deformed specimen after stretching.

of the planar and uniaxial tests, the comparison with the four-process Eyring model may be considered good with the parameter set fixed from only the uniaxial stretching force tests. The hyperelastic model does remarkably well at predicting the overall levels, but key features such as the rise rate and stretch at peak stress are only predicted well by the Eyring model.

Figure 16 shows the back plane of the 3D mesh used for simulation before and after deformation. Overall shape is "similar" to the experimental deformation, but is not obvious from this alone whether the detailed deformation is well predicted. Figure 17 shows a photograph of $\frac{1}{4}$ of the predeformed specimen, and the same photograph numerically deformed according to the finite element solution for the multiprocess Eyring model; the numerical deformation is performed using the method given in the next section [summarized by eq. (37)]. The experimental result shows variation in all four quadrants with the upper right appearing most similar to simulation. The four process Eyring simulation and experiment show great similarity. The large axial stretch ratios between supports are close (measurement gives around 5.2 by simulation compared with 5.4 by experiment), and a much reduced stretch in the areas with supports transversely supporting them. This reduction is more pronounced experimentally than in simulation; experimental stretch ratios are ~ 1.2 in the "supported" areas compared with around 2.4 in simulation. It is clear that the photograph deforming method is effective in identifying full-field similarities and differences between simulation and experiment. The overall comparison of the constitutive model, when applied without parameter change to a significantly different deformation regime is seen to be good, although not perfect when stretch between the supports is considered. The two process Eyring model (parameter set in Table IV) gave similar deformation to the four process model against this problem, with similar variation of stretch around the supports. The corresponding result for the hyperelastic model is shown in Figure 18. The stretching follows a different pattern to experiment with necking being fairly constant across supported and unsupported regions. The hyperelastic model hasn't captured the "intermittent" pattern seen in experiment, and predicted by the Eyring simulations. It is clear that much more realistic predictions are available from the use of the multiprocess Eyring model.

NUMERICALLY DEFORMING DIGITAL PHOTOGRAPHS OF A TEST SPECIMEN

This section gives the method used for numerically deforming a photograph of a specimen, taken before

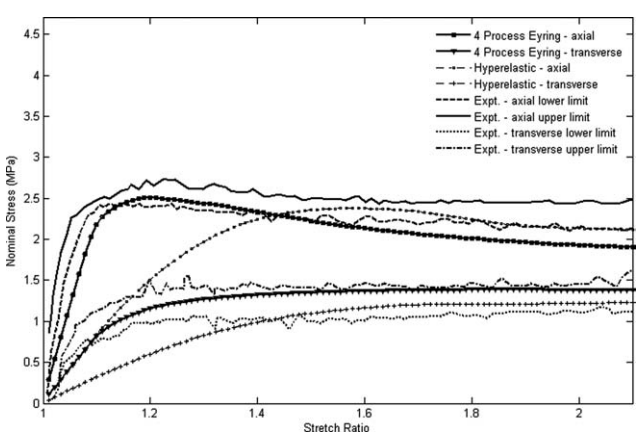

Figure 15 Comparison of experimental axial and transverse stresses with simulation.

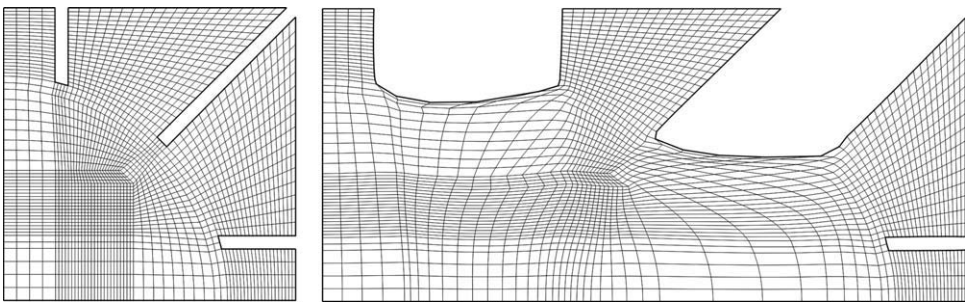

Figure 16 Back plane of 3D mesh before deformation (left) and after deformation (right).

deformation, according to the predictions of a finite element solution.

Consider a digitized photograph of the undeformed specimen comprising many pixels, with a given pixel (identified by index j) having an intensity P_j. Consider that a finite element solution of the geometry is also available, where $\mathbf{X}$ represents the positions of the undeformed mesh, and $\mathbf{X} + \Delta\mathbf{X}(\mathbf{X})$ is the position of the mesh after deformation; $\Delta\mathbf{X}(\mathbf{X})$ is the displacement from position $\mathbf{X}$ given by the finite element solution.

We require a deformed image Q, comprising pixels Q_k such that:

$$\boldsymbol{Q}_k = \sum_{\text{all } i} \boldsymbol{P}_i \boldsymbol{W}_{ik} \tag{35}$$

where W_{ik} is a weight value for the mapping between pixel i of the undeformed image, and pixel k of the required image. To a first estimation the weight could be unity if the position represented by $P_i(\mathbf{X})$ is in the area covered by pixel Q_k after deformation, and zero if it is outside the area of Q_k. A problem of directly implementing this is that there would be some pixels in the deformed image Q_k that had contributions from several pixels P_i, and some Q_k that had none, giving a poor image quality (the problem is similar to the well known problem occurring in image rotation using "forward mapping," but is much exacerbated by the large increase of area in the stretched material). To reduce this affect to acceptable levels a number of integration points are introduced into each pixel P_i. A simple integration scheme was used with equally weighted integration points distributed on a regular $n \times n$ grid within pixel P_i (as indicated in Fig. 19), each integration point represents a (pixel) area of $1/n \times n$, and thus is given that value as an integration weight. This gives a much better quality deformed image defined by:

$$\boldsymbol{Q}_k = \sum_{\text{all } i} \sum_{\text{all } j} \boldsymbol{P}_i \boldsymbol{W}_{ijk}, \tag{36}$$

which incorporates summation over each integration point, j, within pixel P_i. W_{ijk} now takes the value of $1/(n \times n)$ if the original position of integration point j in pixel i moves to the area covered by pixel Q_k after deformation, and zero if it is outside the area of Q_k. Figure 19 represents the mapping of integration points from a pixel P_i before deformation, to several pixels in Q after deformation.

Using an intensity scale where 0 = black and 1 = white, an effect of the above algorithm is to darken stretched areas, since pixels in the stretched areas tend to be spread over greater area when deformed. In the photographs of physical experiments, highly stretched areas actually brighten, including (significantly) the black grid lines etched on the test specimen. A matching thinning effect is achieved by

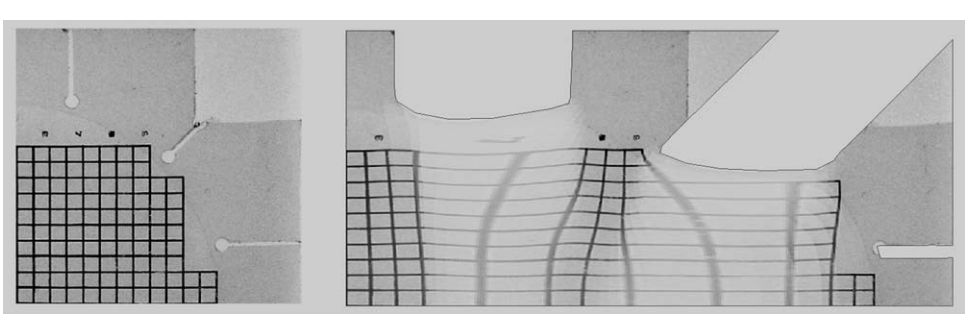

Figure 17 Photograph showing 1/4 of biaxial specimen before stretching, and same photograph deformed according to multiprocess Eyring solution.

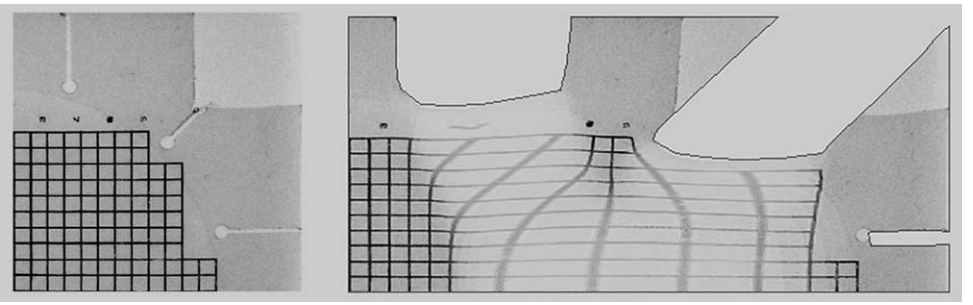

Figure 18 Photograph showing 1/4 of biaxial specimen before stretching, and same photograph deformed according to hyperelastic simulation solution.

calculating the negative of Q_k from the negative of P_i, i.e.

$$\overline{Q}_k = \sum_{\text{all}i} \sum_{\text{all}j} \overline{P}_i W_{ijk}, \tag{37}$$

where $\overline{P}_i = 1 - P_i$. This was used in the artificially deformed images shown in the previous section, using 144 integration points per pixel (i.e., a 12 × 12 integration point grid).

As the image processing is essentially a 2D process it is perhaps better to use explicit (x, y) notation at this point. To make the computation of Q faster, a 2D grid was constructed from the originally flat plane of the 3D mesh. In the current simulation this was done by detecting those nodes at "z = 0;" this corresponds to the plane on which the grid was printed. The most involved part of the computation was finding the element and natural coordinates (r and s) corresponding to the Cartesian coordinates (x and y) of a given integration point. This is necessary so that the displacements at x and y($\Delta x(x,y)$ and $\Delta y(x,y)$) can be calculated from interpolation of nodal solution variables. The first stage is to find those elements (usually one, sometimes two) in which the minimum and maximum x and y values of its nodes enclose the (x_j, y_j) position of integration point j. The elements natural coordinates (denoted by r and s) corresponding to (x_j, y_j) were then found using a few iterations of a Newton's Approximation method given in Appendix. If these (r,s) values are inside the normal range (typically within the bounds of ±1) then that element is the one containing the integration point.

Having the element that the point is in and natural coordinates r and s, the displacements at the position of the integration point can be obtained by standard (finite element) interpolation of solution variables, and the coordinates that it moves to after deformation can be determined; it is then straightforward to locate the corresponding pixel Q_k in a rectangular output image.

DISCUSSION AND CONCLUSIONS

The single process Eyring model was found capable of giving necking behavior with 'small' values of the plastic flow parameter "A." With this small value of A the change in peak stress with rate could be matched, but the simulated pulling force followed a different pattern to experiment. A much larger value

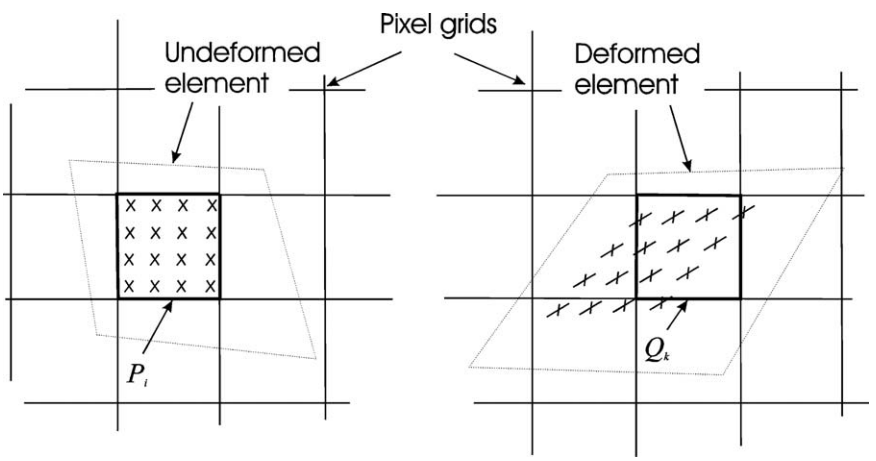

Figure 19 Mapping of pixel integration points from undeformed mesh and image (left) to deformed mesh and image (right).

of "*A*" matched the stretching forces very well at one extension rate, but greatly over-predicted the rise in peak stress with rate, and did not give necking. These last two points appear to be closely linked, since high local rates of extension are associated with necking, and a disproportionate rise in stress will tend to inhibit the local stretching, and thus inhibit necking. With the multiprocess formulation, all of nominal stress, necking, and rate dependence could be matched for the uniaxial tensile specimen. It is possible to criticise a "multimode" model as relying on a relatively large number of adjustable parameters (rather than being guided by specific structural mechanisms, which may give a good fit with fewer adjustable parameters). However the model is extremely flexible, and should be capable of fitting a wide range of polymeric materials with different constitutive structures. The parameter set used was based upon a fit to only the nominal stress measurement for the uniaxial test specimen; the simulation then successfully predicted the stretch measurements along the test specimen. On testing the same material model and parameter set against the same material in a significantly different geometry and extension regime, it was able to predict the "intermittent" stretching nature well with accurate stretch ratios in the highly stretched areas and a good prediction of axial and transverse drawing forces.

The importance of using as low a value for the pressure penalty term (β) was underlined. The minimum value which allowed the planar simulation to reach the end of deformation without mesh failure was 10 (8 gave failure); a value of β of 100 gave little of the "intermittent" stretch behavior, and 300 gave a roughly constant stretch ratio between pulling ends showing none of the observed 'intermittent' stretch. The reason seems related to the degree of "mesh locking," which increases with β; this restricts how the simulation can follow the behavior indicated by the constitutive model.

The multiprocess Eyring model gave much more realistic results than the hyperelastic model: in matching nominal stress values, in retaining the plastic deformation after release, and in matching deformation and drawing forces when transferred to simulation of a significantly different geometry and deformation. The multiprocess Eyring model does not address the specific molecular and crystalline properties within a material directly, but it is inherently flexible, allows controllable rate dependence, and should be capable of useful application to a wide range of processes and materials involving plasticity.

The method for numerically deforming digital photographs/scans of a predeformed specimen by the finite element solution was shown effective in highlighting differences and similarities to experiment. For the large stretches involved a 12 × 12 pixel integration scheme was used to give a smooth output image without noticeable artefacts. The method is very effective in revealing overall strengths and weaknesses of the model in predicting final form, and represents a powerful and challenging test method for large deformation validation.

APPENDIX: NEWTON'S APPROXIMATION BASED METHOD TO LOCATE NATURAL ELEMENT COORDINATES CORRESPONDING TO A CARTESIAN POSITION (X_J, Y_J)

Starting with a central estimation of the values of r and s (both zero), a value of the actual Cartesian coordinates (x_e, y_e) for this (r, s) pair is calculated from standard finite element interpolation:

$$x_e = \sum \psi_m x_m;\ y_e = \sum \psi_m y_m,$$

where ψ_m are the element interpolation functions, and x_m are the nodal values of the element in question. The difference from (x_e, y_e) gives the error in x and y (δx and δy)

$$\begin{bmatrix} \delta x \\ \delta y \end{bmatrix} = \begin{bmatrix} x_j - x_e \\ y_j - y_e \end{bmatrix}.$$

New trial values of r and s can now be found from adding the Newton's Approximation corrections, δr and δs, given by

$$\begin{bmatrix} \delta r \\ \delta s \end{bmatrix} = \mathbf{J}^{-\mathbf{T}} \begin{bmatrix} \delta x \\ \delta y \end{bmatrix},$$

where $\boldsymbol{J}$ is the standard finite element mapping Jacobean for 2D given by

$$\mathbf{J} = \begin{bmatrix} \dfrac{\partial x}{\partial r} & \dfrac{\partial y}{\partial r} \\ \dfrac{\partial x}{\partial s} & \dfrac{\partial y}{\partial s} \end{bmatrix}.$$

The procedure iterates using the updated (r, s) coordinates, until the error in x and y is sufficiently small.

References

1. Gent, A. N.; Jeong, J. Polym Eng Sci 1986, 26, 285.
2. Leonov, A. I. Int J Solids Struct 2002, 39, 5913.
3. Ball, R. C.; Doi, M.; Edwards, S. F.; Warner, M. Polymer 1981, 22, 1010.
4. Sweeney, J.; Collins, T. L. D.; Coates, P. D.; Ward, I. M. Polymer 1997, 38, 5991.
5. Olley, P. Int J Num Meth Eng 2006, 65, 1068.
6. Tvergaard, V. Comp Meth Appl Mech Engng 1993, 103, 273.
7. Masud, A. Int J Num Meth Eng 2000, 47, 1887.

8. Rodriguez-Ferran, A.; Perez-Foguet, A.; Huerta, A. Int J Num Meth Eng 2002, 53, 1831.
9. Arruda, E. M.; Boyce, M. C.; Quintus-Bosz, H. Int J Plast 1993, 9, 783.
10. van Melick, H. G. H.; Govaert, L. E.; Meijer, H. E. H. Polymer 2003, 44, 3579.
11. Sweeney, J.; Collins, T. L. D.; Coates, P. D.; Duckett, R. A. J Appl Polym Sci 1999, 72, 563.
12. Spathis, G.; Kontou, E. Polym Eng Sci 2001, 41, 1337.
13. Nanzai, Y. J Cryst Solids 1991, 131–133, 516.
14. Bitman, L.; Choi, Y.; Choi, S. B.; Werely, N. M. Smart Mater Struct 2005, 14, 237.
15. Tinker, D.; Lesher, C. E.; Baxter, G. M.; Uchida, T.; Wang, Y. Am Mineral 2004, 89, 1701.
16. Buckley, C. P.; Jones, D. C. Polymer 1995, 36, 3301.
17. Llana, P. G.; Boyce, M. C. Polymer 1999, 40, 6729.
18. Boyce, M. C.; Parks, D. M.; Argon, A. S. Mech Materials 1988, 7, 15.
19. Sweeney, J.; Spares, R.; Caton-Rose, P.; Coates, P. D. J Appl Polym Sci 2007, 106, 1095.
20. Sweeney, J.; Spares, R.; Woodhead, M. A. Polym Eng Sci 2009, 49, 1902.
21. Naz, S.; Sweeney, J.; Coates, P. D. J Mater Sci 2010, 45, 448.
22. Sweeney, J.; Naz, S.; Coates, P. D. J Appl Polym Sci 2009, 111, 1190.
23. Belytschko, T.; Liu, W. K.; Moran, B. Nonlinear Finite Elements for Continua and Structures; Wiley: Chichester, 2000.
24. Chandrasekharaiah, D. S.; Debnath, L. Continuum Mechanics; Academic Press Ltd: London, 2000.
25. Kopp, J. Int J Mod Phys 2008, 19, 523.
26. Viriyayuthakon, M.; Caswell, B. J Non-Newt Fluid Mech 1980, 6, 245.